

Journal of Biomedical Optics

BiomedicalOptics.SPIEDigitalLibrary.org

Combining energy and Laplacian regularization to accurately retrieve the depth of brain activity of diffuse optical tomographic data

Antonio M. Chiarelli
Edward L. Maclin
Kathy A. Low
Kyle E. Mathewson
Monica Fabiani
Gabriele Gratton

SPIE.

Antonio M. Chiarelli, Edward L. Maclin, Kathy A. Low, Kyle E. Mathewson, Monica Fabiani, Gabriele Gratton, "Combining energy and Laplacian regularization to accurately retrieve the depth of brain activity of diffuse optical tomographic data," *J. Biomed. Opt.* **21**(3), 036008 (2016), doi: 10.1117/1.JBO.21.3.036008.

Combining energy and Laplacian regularization to accurately retrieve the depth of brain activity of diffuse optical tomographic data

Antonio M. Chiarelli,^a Edward L. Maclin,^a Kathy A. Low,^a Kyle E. Mathewson,^b Monica Fabiani,^a and Gabriele Gratton^{a,*}

^aUniversity of Illinois, Beckman Institute, 405 North Mathews Avenue, Urbana, Illinois 61801, United States

^bUniversity of Alberta, Department of Psychology, P217 Biological Sciences Building, Edmonton, Alberta T6G 2E9, Canada

Abstract. Diffuse optical tomography (DOT) provides data about brain function using surface recordings. Despite recent advancements, an unbiased method for estimating the depth of absorption changes and for providing an accurate three-dimensional (3-D) reconstruction remains elusive. DOT involves solving an ill-posed inverse problem, requiring additional criteria for finding unique solutions. The most commonly used criterion is energy minimization (energy constraint). However, as measurements are taken from only one side of the medium (the scalp) and sensitivity is greater at shallow depths, the energy constraint leads to solutions that tend to be small and superficial. To correct for this bias, we combine the energy constraint with another criterion, minimization of spatial derivatives (Laplacian constraint, also used in low resolution electromagnetic tomography, LORETA). Used in isolation, the Laplacian constraint leads to solutions that tend to be large and deep. Using simulated, phantom, and actual brain activation data, we show that combining these two criteria results in accurate (error <2 mm) absorption depth estimates, while maintaining a two-point spatial resolution of <24 mm up to a depth of 30 mm. This indicates that accurate 3-D reconstruction of brain activity up to 30 mm from the scalp can be obtained with DOT. © 2016 Society of Photo-Optical Instrumentation Engineers (SPIE) [DOI: 10.1117/1.JBO.21.3.036008]

Keywords: 3-D reconstruction; functional brain mapping; near infrared spectroscopy; diffuse optical tomography; minimum-norm; Laplacian regularization, low resolution electromagnetic tomography.

Paper 150805R received Dec. 2, 2015; accepted for publication Feb. 22, 2016; published online Mar. 18, 2016.

1 Introduction

Diffuse optical tomography (DOT) uses near-infrared light (NIR, spectral range 650 to 950 nm) to image three-dimensional (3-D) local changes in light absorption in brain tissue caused by fluctuations in brain oxygenation associated with neuronal activity.¹⁻³ Early studies demonstrated the feasibility of detecting these brain hemodynamic responses *in vivo*^{4,5} and typically relied on sparse arrays of light sources and detectors placed on the scalp surface. In such cases, the spatial resolution parallel to the scalp surface was comparable to the source–detector distance used and no depth information could be recovered. However, current technology allows for high-density arrays of sources and detectors to be placed on the scalp. When applied to high-density optode arrays, DOT relies on multiple overlapping measurements and has the theoretical capability of reconstructing volumetric images of hemodynamic brain activity, greatly improving spatial resolution.⁶⁻¹¹

Despite these technical advances, DOT also has some limitations with respect to 3-D reconstruction. Physical limitations in image reconstruction outcomes are caused by the highly scattering properties of brain tissue, with a minimum point-spread function of ~15 mm.¹² In addition, given the size and contour of the human head, reflectance geometry is widely used, as sources and detectors (i.e., channels, or optodes, or source–

detector pairs) are placed on the same side of the scalp surface. However, photon density decreases exponentially with increasing depth, which translates into limitations in the sensitivity of intensity measurements to deep absorption changes. That makes NIR-DOT measurements hypersensitive to hemodynamic fluctuations occurring in the scalp and sets a practical limit to the maximum depth sensitivity obtainable in real measurements (~30 mm from the recording surface).¹³⁻¹⁵ Finally, there are also mathematical limitations due to the highly underdetermined system involved in the image reconstruction process (as brain voxels greatly outnumber the recording channels).

Mathematically, 3-D reconstruction can be viewed as including two components: building a forward model and finding an inverse solution. The forward problem consists of estimating a sensitivity matrix describing the way intracranial signals (absorption changes at each location inside the head, expressed as a vector) contribute to the data observed at each scalp channel (light intensity changes, also expressed as a vector). The inverse problem refers to the same general equation, in which, however, the task is to determine the vector of intracranial phenomena that can account for the vector of observed scalp values given a particular sensitivity matrix.

A problem with this logic is that, in principle, this sensitivity matrix can change depending on the variations in absorption and scattering observed at each location of the head. Thus, solving the forward problem requires knowing the solution to the

*Address all correspondence to: Gabriele Gratton, E-mail: grattong@illinois.edu

inverse problem (which, however, requires having first solved the forward problem). This creates a complex circular situation requiring, as a minimum, an iterative process for finding solutions. Fortunately, most physiological changes in absorption and scattering over time are very small (<5%), with the consequence that the sensitivity matrix remains almost identical over time. Assuming that this matrix is constant over time allows for the separation of the forward and inverse problems, greatly simplifying the mathematics (i.e., “linearization” of the problem). Standard brain DOT is based on this approach.

In this paper, we will also make this assumption. Further, we will not be concerned with how to best compute the forward model, but we will rather focus on the issue of optimizing inverse solutions for DOT. However, computation of inverse solutions and 3-D reconstruction does require the computation of forward solutions and sensitivity matrices. Therefore, we estimated forward solutions and sensitivity maps using the finite-element method (FEM), which is a commonly used approach.¹⁶

Even when knowing the forward solution and the sensitivity matrix, solving the inverse problem generates significant issues. Specifically, we need to estimate a large number of values inside the head from a relatively small number of scalp locations (which creates an “ill-posed” problem). Further, as mentioned, the geometry of the recordings is unbalanced, as all optical sensors are located on the surface of the head, whereas the effects we need to estimate are all inside the head. This creates the problem of extrapolating the depth of the phenomena inside the head, a problem that is inherently more difficult than interpolating the position of a source occurring in between recording points observed on the surface of the head. This unbalance generates a risk for systematically under- or overestimating the depth of the phenomena causing the surface effects.

The most common method to address illposedness in DOT is the energy-regularized minimum norm solution (ER-DOT). This algorithm favors solutions with small amplitude/energy. ER-DOT is, in fact, consistent with the linearization of the problem (i.e., the actual changes need to be small in order for the linearization to hold), but it results in systematic errors in depth estimation.^{17,18} Specifically, ER-DOT tends to underestimate the depth of activation due to the greater sensitivity for superficial than for deep absorption (or scattering) changes. Hence, a small phenomenon occurring close to the surface can approximate the effect obtained by a much larger phenomenon occurring deep into the medium. As the minimum norm rewards solution with less total energy, the superficial solution is preferred.

This problem can be somewhat reduced, but not fully eliminated, by changes in both the recording montage and the postprocessing procedures. Changes in the montage involve increasing the number of overlapping channels (the more the better, because the problem will become less underdetermined) and including longer source–detector distance recordings. However, in practice, the number of overlapping channels is limited by instrumentation costs, the limited extent of the scalp surface, and the dynamic range of the detectors, whereas the maximum source–detector distance is limited by light attenuation and detector sensitivity (~60 mm).¹² Thus, corrective procedures are also needed to help overcome the depth localization problem when ER minimum-norm algorithms are used.

Two categories of correction algorithms have been developed to address these issues. The first relies on a hybrid image reconstruction method that constrains DOT solutions using anatomical information from magnetic resonance imaging

(MRI).^{18–21} These methods force the solution to lie within the brain of the subject, assume absence of superficial interference, and generally favor estimates of absorption changes on the brain structures closest to the scalp surface, thus not completely addressing the shallow-depth bias.

The second category of algorithms is based on differentially weighting the sensitivity matrix before calculating the inverse solution so as to intentionally overestimate sensitivity to deeper locations. However, with this approach, the inversion procedure loses stability and/or the sensitivity matrix may become distorted, complicating the estimation of the optical changes.^{6,22–27} Moreover, depending on the algorithm employed, additional parameters may need to be tuned.

Another way to address the problem of shallow-depth bias in source estimation is to change the norm used to regularize the inverse solution so as to reflect other important constraints (rather than minimum energy) posed by diffusion physics. One such constraint is that the diffusion process leads to a loss of spatial resolution as depth of the perturbation process increases. This, in turn, leads the surface data to be more sensitive to deep activity that extends in space (in other words, that is, smoother over space) in comparison to very localized activity, which instead changes abruptly over even small distances. A norm that reflects this physical constraint is one that minimizes the spatial gradients (i.e., discrete spatial derivatives or Laplacians) of the brain activity to be reconstructed. As this norm better matches the physics of the diffusion process, it may be expected to produce a more faithful 3-D reconstruction of the data. Unfortunately, compared to ER solutions, Laplacian ones tend to be physically meaningless when the values within the sensitivity map get particularly small. Thus, a combination of energy and Laplacian minimization may provide an optimal solution for the inverse problem.

The Laplacian minimum norm algorithm (low resolution electromagnetic tomography, LORETA) has been widely used for other neuroimaging techniques, like electroencephalography (EEG) and magnetoencephalography (MEG).^{28–30} This approach recognizes the fact that EEG and MEG are mediated by a process (volume conduction) that limits their spatial resolution. As such, they may not be able to detect sudden spatial variations in activity. This problem is akin to photon diffusion, which similarly limits the spatial resolution of DOT, albeit to a lesser extent due to the exponential decay of light gradients over space. As a consequence of the gradient minimization, the LORETA approach favors solutions that are diffuse over space (i.e., smooth), and relatively large. Note that a few large and smooth phenomena occurring at some depth can produce effects that are similar to those of several small superficial effects. This contrasts sharply with the minimum-norm criterion and may be biased toward finding deep solutions of the inverse problem.

In order to reduce bias in either direction, in this paper, we tested a novel algorithm (ELR-DOT) combining energy and Laplacian regularization procedures, and compared it to pre-existing energy regularization methods on simulated and phantom data. Both homogeneous slab geometry and heterogeneous head models were employed. The feasibility of the procedure was finally tested on actual brain activation data collected on one subject undergoing visual stimulation varying in eccentricity. The results suggest that the algorithm produces estimations of the depth of functional activation in the brain that closely correspond to those obtained with functional magnetic resonance imaging (fMRI) in the same subject.

2 Methods

In this paper, we report four sets of data assessing the accuracy of depth and 3-D reconstruction obtained with different types of inverse solutions. These data included: (a) simulated data in which small localized perturbations in the absorption coefficient $\Delta\mu_a(\vec{r})$ were introduced at various depths from the surface of a homogeneous slab medium; (b) simulated data in which small localized perturbations in the absorption coefficient $\Delta\mu_a(\vec{r})$ were introduced at various depths from the surface of a realistic head model; (c) actual data from measurements obtained in a phantom in which a small localized absorbing object was placed at different depths within a homogeneous medium (a milk tank); (d) actual data from a visual stimulation experiment in which the eccentricity of visual stimulation was manipulated to generate activity in occipital brain locations varying in depth from the surface. In the first three cases, the accuracy of the depth and 3-D reconstruction estimates obtained with the various types of inverse solutions was evaluated by comparing it with the known localization and extent of the absorbing objects (simulated or real). In the fourth case, the accuracy of the estimate was evaluated by comparing optical data with fMRI data obtained in the same experiment (considered here the gold standard among brain imaging methods in terms of localization power).

2.1 Forward and Inverse Problems

The goal of image reconstruction (inverse problem) is the recovery of properties of the investigated object for a given recording pattern. For functional NIR DOT, the property of interest is the optical absorption perturbation $\Delta\mu_a(\vec{r})$ over time at each position in space (\vec{r}) using measurements of light intensity from the head surface, from which changes in the concentration of oxy- and deoxyhemoglobin can be computed (provided that multiple wavelengths are used). Previous research has shown that NIR light propagation in highly scattering biological tissue (such as the human head, for which the reduced scattering coefficient is $\mu'_s \gg \mu_a$), is well approximated by the diffusion equation.³¹ According to this equation, the diffusion of light in tissue depends on its baseline optical properties for each location $\mu_a(\vec{r})$, $\mu'_s(\vec{r})$. In complex media such as the head, the diffusion model can be solved using FEM,³² in which continuous variations of optical parameters in space are approximated by discrete changes occurring at finite nodes located at small distances from each other. Importantly, when using FEM to solve the diffusion equation, the optical parameters for each node have to be known. This generates a circularity, because in order to compute the absorption coefficient change at a particular location $\Delta\mu_a(\vec{r})$, we must first know the base value of the absorption coefficient $\mu_a(\vec{r})$ for all locations in the medium, including the one being estimated (a similar problem exists for the scattering coefficient). Thus, the problem is not linear:³³ a change in the recorded pattern due to N perturbations occurring at the same time in different positions is not equal to the sum of the changes in the recording pattern due to each perturbation occurring separately. This issue is important when the perturbations are large and require computing absolute optical parameters. In this case, iterative processes need to be employed. Multiple algorithms have been developed that rely on different iterative procedures and regularizations.^{33–35} They are generally applied to frequency-domain data and show promising results.

In the case of relative changes due to physiological factors, this apparent conundrum can be solved by considering that the changes in absorption (or scattering) related to brain activity are small with respect to the base value (1% to 5% for oxygenation, with the expected changes in scattering being even smaller) and can therefore be ignored as a first approximation when describing the diffusion of light through tissue. The issue of estimating local changes in $\Delta\mu_a(\vec{r})$ can then be isolated from that of how light diffuses (linearization). This means that we can assume that the baseline optical properties of the tissue are not sufficiently changed as a function of brain activity to require us to update the light diffusion model to include such changes. We can therefore estimate a light diffusion model only once without having to iterate the process to include the effects of the changes due to local perturbations to the basic model. This linearized model is mathematically described by a matrix (sensitivity, or Jacobian, matrix) describing the effects on the light intensity measured by optodes located on the medium surface as a function of unitary absorption perturbations at any location inside the medium (forward model):

$$\Delta\text{OD} = \mathbf{J}_{[\mu_a(\vec{r}), \mu'_s(\vec{r})]} \Delta\mu_a(\vec{r}), \quad (1)$$

where ΔOD is the logarithm of the proportional change in intensity due to a local variation in absorption $\Delta\mu_a(\vec{r})$ for each channel (i.e., optical density). Note that ΔOD is a vector of optical density changes for each channel, and $\mathbf{J}_{[\mu_a(\vec{r}), \mu'_s(\vec{r})]}$ is a rectangular $n \times m$ matrix, where n is the number of channels, m is the number of space positions considered (number of mesh nodes when FEM is used), and $\Delta\mu_a(\vec{r})$ is a vector of absorption perturbations for each location: the values for each cell of the rectangular matrix \mathbf{J} (also called Jacobians) are estimated using an FEM procedure. Generally, $n \ll m$.

2.2 Computation of the Forward Light Model: Finite-Element Method

In our forward model computation, a fine mesh (maximum tetrahedral volume = 2 mm³) was generated for FEM using the software iso2mesh³⁶ for both slab geometry (used for the simulated and actual milk-tank data) and heterogeneous models of the head (used for the simulated and actual brain imaging data). Heterogeneous models require segmentation of a structural MR image of the subject's head into skull and scalp, cerebrospinal fluid (CSF), white matter, and gray matter, which was performed using statistical parametric mapping (SPM) functions applied to T1 structural images.³⁷ Baseline optical properties (absorption parameter μ_a , reduced scattering μ'_s , and refraction index η) of the tissues at the relevant wavelengths (830 nm) were taken from Tian and Liu.²⁷ Given the similarities of optical properties of skull and scalp and the difficulty of separating them in T1 images, we decided to attribute the same optical property values to both structures. Specifically, the values were set equal to those reported for the skull (see Table 1 for the actual optical values used).

The FEM software NIRFAST³³ was used to model light propagation through the medium. NIRFAST was used to compute the boundary data for a given optode montage when simulations were employed. Finally, NIRFAST was also used to compute the sensitivity (Jacobian) matrices for both simulated and real data using the adjoint method.³⁸

Table 1 Optical properties for different types of tissues (830 nm wavelength, from Tian and Liu²⁷).

Tissue type	Absorption (μ_a in mm^{-1})	Reduced scattering (μ'_s in mm^{-1})	Refraction index
Scalp and skull	0.014	0.84	1.4
CSF	0.004	0.30	1.4
Gray matter	0.019	0.67	1.4
White matter	0.021	1.01	1.4

2.3 Inverse Modeling: Energy, Spatially Variant, and Laplacian Regularized Minimum Norm

The inverse problem requires solving Eq. (1) for $\Delta\mu_a(\vec{r})$ based on a known ΔOD (the change in optical density measured at each channel) and J (the Jacobian matrix). However, $J_{[\mu_a(\vec{r}), \mu'_s(\vec{r})]}$ is generally not square, and therefore cannot be inverted (generating the well-known ill-posedness of inverse problems). In order to provide a unique and stable solution to the inverse form of Eq. (1), further constraints need to be made (norms). Least squares estimation and energy regularization are the most common procedures employed (generally using the ℓ_2 , or Euclidean, norm).³⁹ In this case, $\Delta\mu_a(\vec{r})$ is estimated by minimizing the function $O[\Delta\mu_a(\vec{r})]$:

$$O[\Delta\mu_a(\vec{r})]J_{[\mu_a(\vec{r}), \mu'_s(\vec{r})]} = \|J_{[\mu_a(\vec{r}), \mu'_s(\vec{r})]}\Delta\mu_a(\vec{r}) - \Delta\text{OD}(n)\|^2 + \varepsilon\|\Delta\mu_a(\vec{r})\|^2, \quad (2)$$

where ε is the energy regularization parameter.

Because the ℓ_2 norm is differentiable and convex, the problem can be solved by differentiating $O[\Delta\mu_a(\vec{r})]$ with respect to $\Delta\mu_a(\vec{r})$ and setting the equation to zero. The following equation, providing a linearized image reconstruction (ER-DOT), is then obtained:

$$\Delta\mu_a(\vec{r}) = J_{[\mu_a(\vec{r}), \mu'_s(\vec{r})]}^T [J_{[\mu_a(\vec{r}), \mu'_s(\vec{r})]} J_{[\mu_a(\vec{r}), \mu'_s(\vec{r})]}^T + \varepsilon I]^{-1} \Delta\text{OD}(n), \quad (3)$$

where I is the identity matrix (here, superscript “T” indicates matrix transposition).

Note that if $\varepsilon = 0$, the problem simplifies to a classic least squares solution, which would provide a 3-D reconstruction with the highest theoretical resolution. However, in most cases, the matrix resulting from the product $J_{[\mu_a(\vec{r}), \mu'_s(\vec{r})]} J_{[\mu_a(\vec{r}), \mu'_s(\vec{r})]}^T$ is almost singular (i.e., the determinant is very close to zero) and the inversion of this matrix leads to unstable results (this practically leads to very noisy 3-D images)—hence, the need for $\varepsilon > 0$. Thus, the parameter ε provides reliable numerical results by trading spatial resolution in data fitting for stability. The increased stability is reached by forcing the unknown to be small.

The optimal value of ε can be found using statistical methods^{40,41} or empirically. In brain DOT, ε is normally found empirically as a value proportional to the maximum of $\|J_{[\mu_a(\vec{r}), \mu'_s(\vec{r})]}\|^2$.^{12,22,23} This means that ε is tuned to a value proportional to the squared Euclidean norm of the Jacobian for

the node where it is the biggest. The practical consequence of this is that the algorithm finds solutions that minimize the mean squared $\Delta\mu_a(\vec{r})$ required, accounting for the observed effects (minimum norm).

As mentioned above, the minimum norm procedure tends to favor lower-energy superficial solutions over larger-energy deep solutions. Several procedures have been developed to address this issue. They mainly rely on weighting the Jacobian as a function of space. Probably the most common procedure in brain DOT is the spatially variant regularization (SVR-DOT) introduced by Culver et al.²² Thus, here, we employ the SVR-DOT algorithm, where $\Delta\mu_a(\vec{r})$ is estimated by minimizing the function $O[\Delta\mu_a(\vec{r})]$:

$$O[\Delta\mu_a(\vec{r})] = \|J_{[\mu_a(\vec{r}), \mu'_s(\vec{r})]}\Delta\mu_a(\vec{r}) - \Delta\text{OD}(n)\|^2 + \varepsilon\|W\Delta\mu_a(\vec{r})\|^2, \quad (4)$$

and W is the SVR matrix.

The linearized image reconstruction (SVR-DOT) is obtained as

$$\Delta\mu_a(\vec{r}) = (W^T W)^{-1} J_{[\mu_a(\vec{r}), \mu'_s(\vec{r})]}^T \times \left[J_{[\mu_a(\vec{r}), \mu'_s(\vec{r})]} (W^T W)^{-1} J_{[\mu_a(\vec{r}), \mu'_s(\vec{r})]}^T + \varepsilon I \right]^{-1} \Delta\text{OD}(n). \quad (5)$$

In order to dampen the effect of decreased sensitivity to deep phenomena, the regularization needs to be increased when the Euclidean norm for a particular node is high and vice-versa. In a general approach, W is a diagonal matrix equal to the $\|J_{[\mu_a(\vec{r}), \mu'_s(\vec{r})]}\|$ for each node at position (\vec{r}) . It can be computed as

$$W = \text{diag}[J_{[\mu_a(\vec{r}), \mu'_s(\vec{r})]}^T J_{[\mu_a(\vec{r}), \mu'_s(\vec{r})]}]^{1/2}. \quad (6)$$

However, this procedure tends to make the solution unstable. In order to address this issue, a spatial regularization parameter β needs to be introduced:

$$W = \text{diag}[J_{[\mu_a(\vec{r}), \mu'_s(\vec{r})]}^T J_{[\mu_a(\vec{r}), \mu'_s(\vec{r})]} + \beta]^{1/2}. \quad (7)$$

Beta is generally chosen to be proportional to the maximum value of $\|J_{[\mu_a(\vec{r}), \mu'_s(\vec{r})]}\|^2$. Tuning the parameter using β produces a trade-off between stability of the linear inversion and ability to reconstruct deep phenomena.

As mentioned above, a possible alternative method to the energy regularization procedure that is suited to correct for the shallow-depth bias is the Laplacian regularization method. This method may, however, introduce an opposite bias toward deep regions of activation. Therefore, here, we introduce a combination of both approaches, the ELR-DOT algorithm, in order to overcome the issue of depth sensitivity without generating a depth bias. With ELR-DOT, the reconstructed image $\Delta\mu_a(\vec{r})$ is estimated by minimizing the function $O[\Delta\mu_a(\vec{r})]$:

$$O[\Delta\mu_a(\vec{r})] = \|J_{[\mu_a(\vec{r}), \mu'_s(\vec{r})]}\Delta\mu_a(\vec{r}) - \Delta\text{OD}(n)\|^2 + \varepsilon\|\Delta\mu_a(\vec{r})\|^2 + \lambda\|L\Delta\mu_a(\vec{r})\|^2, \quad (8)$$

where L is the Laplacian operator, ε is the energy regularization parameter, and λ is the Laplacian regularization coefficient.

In the current paper, this parameter was selected based on simulations on a slab geometry model and then used unchanged for all other datasets. In a 3-D space and for a regular cubic grid of nodes, the discrete Laplacian can be approximated using Dirichlet boundary conditions, such that

$$\nabla^2[\Delta\mu_a(\vec{r})] = 6[\Delta\mu_a(\vec{r})] - \sum_p \Delta\mu_a(\vec{r}_p), \quad (9)$$

for each p under the constraint: $\|\vec{r}_i - \vec{r}_p\|^2 = d$, where ∇^2 is the Laplacian operator for the position \vec{r}_i . With this definition, matrix L is symmetric, nonsingular, and sparse.²⁹ On the assumption of $\varepsilon > 0$, the linearized image reconstruction (ELR-DOT) is obtained as

$$\begin{aligned} \Delta\mu_a(\vec{r}) &= \left(I + \frac{\lambda}{\varepsilon} L^T L \right)^{-1} \mathbf{J}_{[\mu_a(\vec{r}), \mu'_s(\vec{r})]}^T \\ &\times \left[\mathbf{J}_{[\mu_a(\vec{r}), \mu'_s(\vec{r})]} \left(I + \frac{\lambda}{\varepsilon} L^T L \right)^{-1} \mathbf{J}_{[\mu_a(\vec{r}), \mu'_s(\vec{r})]}^T + \varepsilon I \right]^{-1} \Delta\text{OD}(n). \end{aligned} \quad (10)$$

To speed up computation and to reduce the number of unknowns in the inversion algorithm, the Jacobians were resampled into a cubic grid with a minimum interposition distance d of 5 mm using NIRFAST. With NIRFAST, the Jacobian matrices can be resampled at any desired isovoxel resolution. A 5-mm resolution for the Jacobian was selected as an optimal value, balancing the need for a high level of detail in the description of the spatial properties of the 3-D model while limiting the illposedness of the problem. In particular, the value chosen (5 mm) provides a spatial frequency that is beyond the Nyquist frequency involved in the DOT reconstruction process (spatial resolution of DOT is around 15 mm).¹² For display purposes, 1-mm-voxel images were reconstructed by cubic spline interpolation of $\Delta\mu_a(\vec{r})$ in node space.

2.4 Metrics

In order to estimate the performance of the ELR-DOT algorithm compared to ER-DOT and SVR-DOT, several different metrics were used. One metric estimated the stability of the algorithm inversion independently of the recorded data. Looking at Eqs. (3), (5), and (10), the linear inversion consists of multiply recorded data $\Delta\text{OD}(n)$ by a matrix that we called G :

$$\Delta\mu_a(\vec{r}) = G\Delta\text{OD}(n). \quad (11)$$

We decided to estimate the algorithm stability by computing the Frobenius norm of matrix G for different regularization parameters and different algorithms. The Frobenius norm is computed as

$$\|G\|_F = \sqrt{\sum_{i=1}^m \sum_{j=1}^n |g_{ij}|} = \sqrt{\text{trace}(G^T G)}. \quad (12)$$

The Frobenius norm tests for the magnitude of the values of the matrix G and, for a given forward solution, is a test of the inverse procedure stability. When the solution is more stable, lower values of $\|G\|_F$ are obtained and vice-versa.⁴²

Other metrics considered were related to the reconstructed images. When a single perturbation was considered, three

metrics were used. The position error (PE) was computed as the difference between the centroid of the known position of a perturbation and the reconstructed one, namely,

$$\text{PE} = \left\| \frac{\sum_{i=1}^n \vec{r}_i \Delta\mu_a(\vec{r}_i)}{\sum_{i=1}^n \Delta\mu_a(\vec{r}_i)} - \vec{r}_{\text{known}} \right\| \quad \text{at } x_{\text{known}}, y_{\text{known}}, \quad (13)$$

For each $\Delta\mu_a(\vec{r}) > 0.5_{\text{max}}[\Delta\mu_a(\vec{r})]$, where \vec{r}_{known} is the known position of the perturbation, n is the number of the nodes, and $\Delta\mu_a(\vec{r})$ is the reconstructed absorption changes. The constraint $\Delta\mu_a(\vec{r}_i) > 0.5_{\text{max}}[\Delta\mu_a(\vec{r})]$ was chosen in order to dampen the effect of small noise in the PE estimation.

The estimated depth (ED) of a reconstructed perturbation was computed as

$$\text{ED} = \left\| \frac{\sum_{i=1}^n \vec{z}_i \Delta\mu_a(\vec{z}_i)}{\sum_{i=1}^n \Delta\mu_a(\vec{z}_i)} \right\| \quad \text{at } x_{\text{known}}, y_{\text{known}}, \quad (14)$$

for each $\Delta\mu_a(\vec{r}_i) > 0.5_{\text{max}}[\Delta\mu_a(\vec{r})]$, where z is the depth coordinate, x_{known} and y_{known} are the known lateral positions of the perturbation, and n is the number of the nodes on the z axis.

In addition, the full-width half-maximum (FWHM) of the reconstructed perturbation was computed. The average FWHM along the three main axes is reported as

$$\text{FWHM} = \frac{\text{FWHM}_x + \text{FWHM}_y + \text{FWHM}_z}{3}. \quad (15)$$

When two perturbations were considered, a value called the resolution parameter (RP) was computed. RP is the ratio between the absorption value at the midway position between the two perturbations and the average value of absorption at the centers of the perturbations:

$$\text{RP} = \frac{2 \left[\Delta\mu_a \left(\frac{\vec{r}_1 + \vec{r}_2}{2} \right) \right]}{\Delta\mu_a(\vec{r}_1) + \Delta\mu_a(\vec{r}_2)}, \quad (16)$$

where \vec{r}_1 and \vec{r}_2 are the known centroid positions of the absorption perturbations and $\Delta\mu_a(\vec{r})$ is the reconstructed image. RP approaches 0 when the two perturbations are clearly identified, <1 when some level of separation exists, and >1 or more when the reconstructed perturbations are fused together.

2.5 Simulations: Slab Geometry

In order to estimate the optimal combination of energy and Laplacian regularization parameters, we ran a simulation considering a homogeneous cubic medium of $100 \times 100 \times 100$ mm, having baseline absorption and reduced scattering coefficients of $\mu_a = 0.01 \text{ mm}^{-1}$ and $\mu'_s = 1 \text{ mm}^{-1}$, respectively. These absorption and reduced scattering coefficients were chosen to represent commonly accepted average values of optical properties in the NIR range⁴³ obtained with *in-vivo* measurements of biological tissues. A square array of optodes (minimum source–detector distance of 15 mm) was arranged on a face of the cube (Fig. 1). Only source–detector distances within 60 mm were considered meaningful. A spherical absorber with a 4-mm radius and $\mu_a = 0.011 \text{ mm}^{-1}$ (10% change from bulk value) was embedded at the center of the investigation surface at different depths (centered from 5 to 35 mm from the recording surface). Gaussian noise amounting to 5% of the maximum

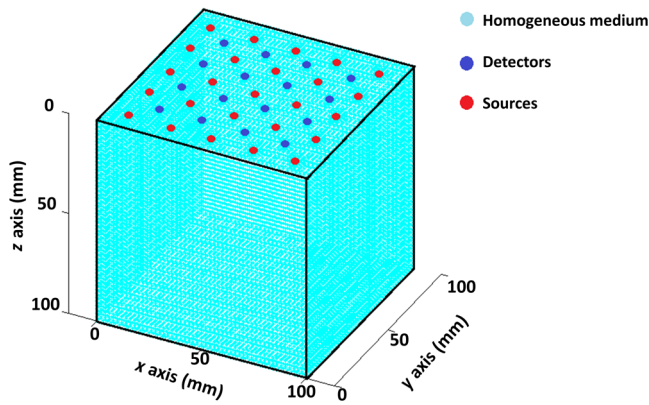


Fig. 1 Homogeneous cubic mesh (100 mm^3) used for simulations and real data image reconstruction. A square array of optodes, with alternating sources and detectors, was arranged over parallel lines at distances of 15 mm on a face of the cube. This same array was also used for the real (phantom) data collected in the milk tank. For both the simulation and the phantom experiments, an absorption perturbation was positioned at the center of the investigation surface at different depths.

intensity change was introduced in the simulation as an initial step to assess the effects of noise on the DOT reconstruction algorithm.³³ Intensities were computed for each meaningful source–detector pair for the different conditions. The optimal energy and Laplacian regularization parameters were estimated by minimizing the maximum PE among the different depths considered (we required the algorithm to be accurate for all those depths). The ELR-DOT regularization algorithm was compared to ER-DOT and SVR-DOT as a function of regularization values using the metrics Frobenius norm, PE, and FWHM.

In order to estimate the resolution capabilities of ELR-DOT, two absorbing perturbations (radius = 4 mm, $\mu_a = 0.011 \text{ mm}^{-1}$) were embedded at a depth of 25 mm, while the distance between them was varied by moving their centers from 10 to 40 mm apart (perturbation distance, PD) in 2-mm steps. The RP metric was evaluated for each PD.

2.6 Simulations: Real-Head Geometry

The robustness of parameter-tuned ELR-DOT to changes in geometry and baseline optical values were tested using a heterogeneous realistic head geometry. The head's geometry and optical values were derived from T1-weighted MR images obtained in five subjects who were recruited and run using procedures approved by the University of Illinois Institutional Review Board. The T1-weighted MR images were acquired with a Siemens Trio[®] 3T scanner using a 3-D MPRAGE (magnetization prepared rapid gradient echo) sequence [repetition time (TR) = 1900 ms, inversion time (TI) = 900 ms, echo time (TE) = 2.32 ms, field of view = $230 \times 230 \times 172.8 \text{ mm}^3$ (sagittal), matrix size = $256 \times 256 \times 192$, flip angle = 9 deg, slice thickness = 0.9 mm]. Single MRI image slices were concatenated and converted into NIFTI format using the dcm2nii conversion tool⁴⁴ called by a MATLAB[®] toolbox. Each image was then placed into a left–right (L-R), posterior–anterior (P-A), inferior–superior (I-S) spatial orientation and resampled into 1-mm isovoxels by cubic spline interpolation of the original image.⁴⁵ Segmentation of the subject's head into skull and scalp, CSF, white matter, and gray matter was performed using SPM functions applied to T1 structural images.³⁷

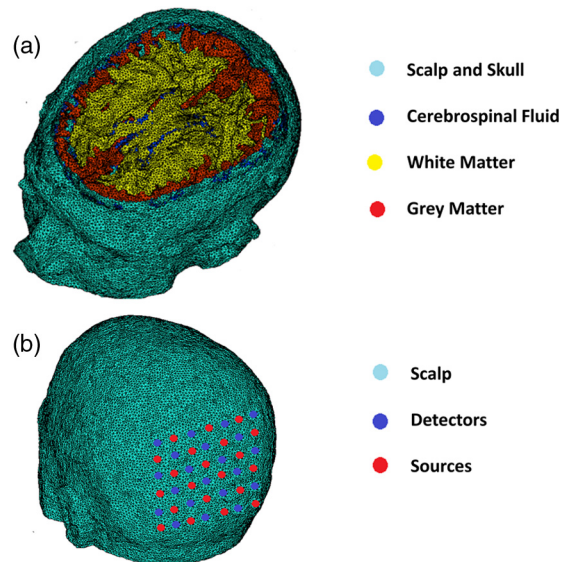


Fig. 2 Example of a heterogeneous head mesh (maximum tetrahedral volume = 2 mm^3) generated for FEM, computed using iso2-mesh. (a) Segmentation divisions of skull and scalp, CSF, white matter, and gray matter, performed on T1 structural images. Different optical properties (see Table 1) were attributed to different tissues. (b) Source and detector locations (same geometry as Fig. 1) on the occipital surface of the head.

A fine mesh (maximum tetrahedral volume = 2 mm^3) was generated for NIRFAST computing using the software iso2-mesh.³⁶ A square array of optodes (minimum source–detector distance = 15 mm) was simulated on the scalp over the occipital cortex of the subjects (Fig. 2). Only source–detector distances within 60 mm were considered meaningful. An absorbing sphere with radius = 4 mm and $\mu_a = 0.011 \text{ mm}^{-1}$ (10% change from bulk value) was embedded in the occipital area at different depths from the scalp (center varying from 3 to 33 mm from the surface). Intensities for the different conditions were computed. Gaussian noise amounting to 5% of the maximum intensity change was introduced in the simulation. ELR-DOT, SVR-DOT, and ER-DOT were applied to the simulated recorded intensities, and ED and FWHM metrics were evaluated using optimum regularization values, determined using the homogeneous slab simulations.

2.7 Phantom Data: Slab Geometry

We also tested the ability of the combination of the FEM forward solver with the ELR-DOT algorithm to reconstruct real changes of local absorption in a homogeneous slab medium using reflectance geometry. Because of the known similarity between the scattering properties of milk and human tissue in the NIR spectral range, homogenized skim milk was used as a bulk substance.⁴⁶ The milk was put in a 4-l black tank and was kept at a constant temperature using ice. India ink was added in order to increase the homogeneous absorption to more closely mimic the overall optical properties of head tissue. Data were acquired with a multichannel frequency-domain commercial NIR spectrometer (ISS Imagent[™], Champaign, Illinois) equipped with 128 laser diodes (64 emitting light at 690 nm and 64 at 830 nm) and 24 photomultiplier tubes. Time multiplexing was employed, so that each detector picked up light from 16 different sources at different times within a multiplexing cycle.

A square array of optodes (minimum source–detector distance = 15 mm) was arranged on the surface of the milk in the same configuration reported in Fig. 1. Baseline absorption values were estimated using the frequency-domain system in a multidistance configuration.⁴⁷ The estimated absorption and scattering values over a recording epoch of 2 min were $\mu_a = 0.0095 \text{ mm}^{-1}$ and $\mu_s' = 0.85 \text{ mm}^{-1}$ at 830 nm.

An absorbing sphere with radius = 3 mm and $\mu_a = 0.02 \text{ mm}^{-1}$, $\mu_s' = 0.95 \text{ mm}^{-1}$ at 830 nm of wavelength was embedded at the center of the investigation surface and moved with a mechanical mechanism to different depths from the milk surface (center varying from 3 to 33 mm from the surface). Data at different depths were acquired for 30 s with a 40-Hz sampling rate. Reference (homogeneous medium) intensities were acquired with the absorber at depth = 40 mm. Reference data were taken for 30 s after each depth recording in order to compensate for slow instrumentation drifts. Data acquired using 830-nm wavelength NIR light were used for image reconstruction. Channels that presented a variation of the intensity >40% for any of the depth recordings when compared to baseline were considered noisy and disregarded during the image reconstruction process. ED and FWHM metrics were estimated for the reconstructed images computed using ELR-DOT, ER-DOT, and SVR-DOT.

2.8 Real (In-Vivo) Data: Eccentricity Study

In order to quantify the ability of ELR-DOT to localize functional activation *in vivo*, we compared results obtained with fMRI and ELR-DOT for one subject performing a visual eccentricity task. The participant was recruited and run with approval from the University of Illinois Institutional Review Board. The visual eccentricity task is particularly suitable for evaluating algorithm localization performance. In fact, it is well known that the visual cortex is spatially organized as a function of the eccentricity (and polar angle) of visual stimulation. More importantly for testing the accuracy of depth estimations, the more eccentric the stimulus, the deeper the areas of the primary visual cortex involved in its processing.^{48–50}

The data reported in this paper are from one participant, who underwent a typical hemodynamic imaging eccentricity study in which a ring comprising a contrast-reversing checkerboard pattern (2 Hz) was presented at the center of the screen and expanded (and in a separate block, contracted) continuously in size, increasing or decreasing the stimulated visual angle.⁵¹ Visual angles from 0 to 10 deg were spanned during the experiment. Within a stimulation period of 48 s, the expanding or contracting cycle was repeated eight times. The stimulus was designed to generate asynchronous responses in regions of the primary visual cortex corresponding to different visual angles, and therefore varying in depth. fMRI data were acquired with a Siemens Trio® 3T scanner using a BOLD sequence (TR = 2000 ms, TE = 25 ms, flip angle = 90 deg, in-plane resolution = $2.5 \times 2.5 \text{ mm}$, slice thickness = 2.5 mm). fMRI images were coregistered to the structural resampled MRI of the same participant, producing a four-dimensional (4-D) time-course image in structural space.

fNIRS data were acquired with a multichannel frequency-domain NIR spectrometer (ISS Imagent™, Champaign, Illinois). Optical data from the same participant were recorded using an array of eight source pairs (830 and 690 nm) and 16 detectors positioned on the scalp over the occipital cortex [with source–detector distances ranging from 20 to 70 mm;

Fig. 11(c)]. The optode array was designed so as to provide coverage of the primary visual cortex, and, most importantly for the purposes of the current paper, to provide a wide variance of source–detector distances over a relatively small surface. As in Ref. 48, this was achieved by grouping all the sources over one hemisphere and all the detectors over the other. Simulations and real-task data indicate that this “grouped” geometry is very effective (compared to a square-grid geometry) in providing a good 3-D reconstruction of perturbations located in between the sources and the detectors. This montage also avoids the problem of having too many short-distance channels, challenging the dynamic range of the detectors. Fiducial markers were placed on the participant’s left and right preauricular points and on the nasion (Na). Fiducials, optodes, and other scalp locations were digitized with a Polhemus FastTrak 3-D digitizer (Colchester, VT; accuracy: 0.8 mm) using a recording stylus and three head-mounted receivers, which allowed for small movements of the head in between measurements. Optode locations and structural MRI data were coregistered using fiducials and a surface-fitting Levenberg–Marquard algorithm.⁴⁵

Only data recorded with the 830-nm wavelength were used for the computation of DOT. Preprocessing involved movement correction,⁵² removal of noisy channels (i.e., channels that presented a variation in intensity greater than 40%), and signal resampling (0.5 Hz). The last step of preprocessing regressed out the shortest channels’ signals from all the good channels in order to dampen the effect of superficial interference.⁵³

After applying ELR-DOT, we obtained an estimate of the absorption changes at 830 nm for each node considered. Nodes with a very small sensitivity were masked (norm equal to 10^{-6} of the maximum norm estimated). A voxel-based image of absorption changes in the head was obtained by cubic spline interpolation of the absorption values in node space.

Because of the increased oxygenation of the brain in active areas and the hemoglobin extinction coefficients at 830 nm of wavelength, changes in absorption at the wavelength of interest should be proportional to the BOLD response of the fMRI. The same statistical analysis in the same structural space (T1 subject MRI space) was conducted on both fMRI data and fNIRS ELR-DOT data.

The 4-D functional images of the two blocks (expanding and contracting rings) were subtracted from one another in order to eliminate the effect of the lag of the hemodynamic response function. Each voxel in the obtained 4-D images was correlated in time with a sine and a cosine of a period of $T = 48 \text{ s}$. As the stimulus varied continuously in eccentricity as a function of time, for both fMRI and fNIRS data, the phase of the hemodynamic response reflected the tuning of the brain activity to a particular stimulus eccentricity. The phase estimate at the particular oscillation frequency (48 s) was obtained for each voxel as

$$\text{Ph}(x, y, z) = \tan^{-1} \frac{\text{corr}[s(x, y, z, t), \sin(2\pi Tt)]}{\text{corr}[s(x, y, z, t), \cos(2\pi Tt)]}, \quad (17)$$

where $s(x, y, z, t)$ is the signal over time at a given voxel x, y, z .

A t -score $t(x, y, z)$ was obtained by correlating the signal in each voxel with a cosine shifted by the amount $\text{Ph}(x, y, z)$, corresponding to each stimulation eccentricity. Knowing the ranges of stimulated visual angles and the time when they occurred,

it was possible to linearly relate $\text{Ph}(x, y, z)$ to visual eccentricity, thus obtaining a $\text{VA}(x, y, z)$, where $\text{VA}(x, y, z)$ was a brain map of the visual angle that maximally stimulated a particular voxel.⁵⁴

fMRI results were smoothed using a Gaussian filter with a $\text{FWHM} = 20$ mm in order to account for the reduced spatial resolution of DOT when compared to fMRI. fMRI and ELR-DOT results were compared by correlating statistically significant voxels ($p < 0.05$) $\text{VA}(x, y, z)$ over space of the two imaging procedures. Here, we report results obtained for a single subject to show feasibility. This subject had particularly robust effects for both fMRI and DOT analysis. Statistical analyses on a bigger sample of subjects will be reported in a separate paper.

3 Results

3.1 Simulations: Slab Geometry

The purpose of the first set of simulations was to estimate the relative weights to be given to the energy and Laplacian regularization matrices (ε and λ) when combining them. In order to better quantify the effects of the regularization parameters ε and λ , the quantity $\mathbf{J}_{[\mu_a(\bar{r}), \mu_s'(\bar{r})]} (I + \frac{2}{3} \mathbf{L}^T \mathbf{L})^{-1} \mathbf{J}_{[\mu_a(\bar{r}), \mu_s'(\bar{r})]}^T$ was set to 0.

Figure 3 reports the channel average inversion matrix G for a slice passing through the middle of and perpendicular to the recording surface for different ratios of ε to λ . For a ratio $\varepsilon/\lambda = 10^4$, the matrix G is almost identical to the forward solver $\mathbf{J}_{[\mu_a(\bar{r}), \mu_s'(\bar{r})]}^T$. This ratio shows the effect of a strongly energy-weighted regularized solver for which the data are forced toward the surface, the region of higher sensitivity. As the ratio of ε to λ decreases, the Laplacian regularization increases its effect, clearly moving the preferential solutions to deeper tissues.

However, when the ratio is very low (i.e., $=10^{-4}$), the operator generates physically unlikely (very deep) solutions (e.g., >5 cm). Thus, Fig. 3 suggests that an intermediate ratio between the two regularization parameters might provide an optimal solution.

The second step of our analysis was to estimate the best ε and λ for ELR-DOT. For comparison purposes, the best ε for ER-DOT and the best ε and β for SVR-DOT were computed. We estimated the best regularization values running forward simulations with perturbations of baseline optical properties, positioned in the homogeneous media at different depths (see Sec. 2). The goal of the optimization was to find the minimum of the maximum PE for all the depths (we wanted accurate results for all the depths considered) given the parameters ε , λ , and β . The values were estimated normalized to the $\max(\|\mathbf{J}_{[\mu_a(\bar{r}), \mu_s'(\bar{r})]}\|^2)$:

$$E = \frac{\varepsilon}{\max(\|\mathbf{J}_{[\mu_a(\bar{r}), \mu_s'(\bar{r})]}\|^2)}, \quad (18)$$

$$\Lambda = \frac{\lambda}{\max(\|\mathbf{J}_{[\mu_a(\bar{r}), \mu_s'(\bar{r})]}\|^2)}, \quad (19)$$

$$B = \frac{\beta}{\max(\|\mathbf{J}_{[\mu_a(\bar{r}), \mu_s'(\bar{r})]}\|^2)}. \quad (20)$$

The analysis was conducted by varying E , Λ , and B from 10^{-7} to 10^{-1} . Similarly to previous studies,^{12,22,23} we found an optimal energy regularization parameter equal to $E = 10^{-5}$. Thus, in order to focus on the effects of the Laplacian regularization and the SVR, here we present results obtained at a fixed energy regularization equal to $E = 10^{-5}$.

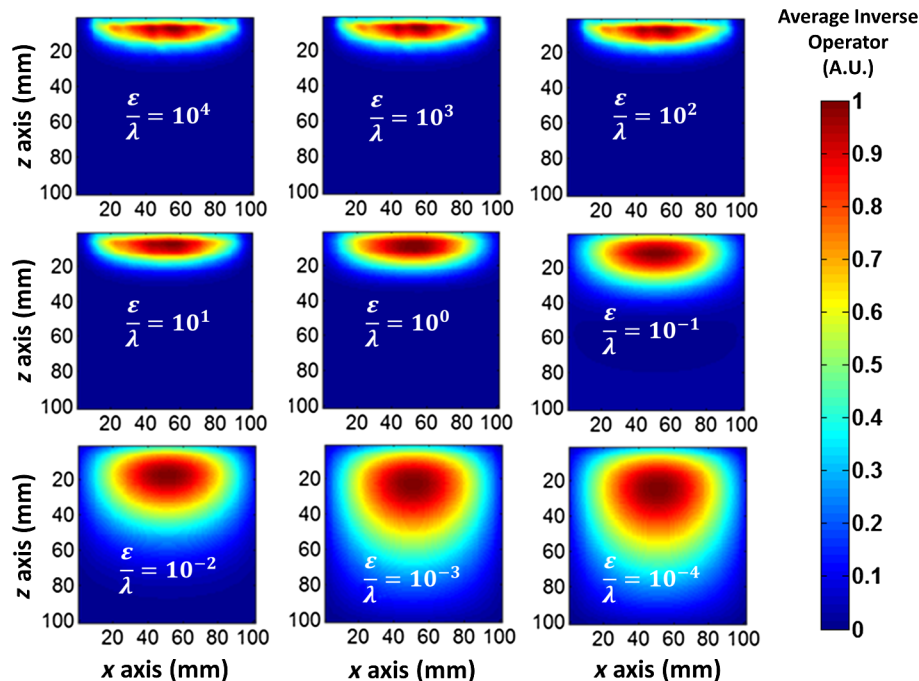


Fig. 3 Channel average inverse operator using cube geometry, presented on a slice perpendicular to the recording surface, passing through the middle of the cube. Different images show a different combination of ratios between ε (energy regularization parameter) and λ (Laplacian regularization parameter). As the ratio between ε and λ decreases, the Laplacian regularization increases its effect, clearly moving the preferential solutions to deeper tissues.

Increasing the value of Λ increases the relative weight given to the Laplacian regularization, whereas decreasing the value of B increases the relative weight given to the spatial regularization. For display purposes, we report a value of spatial regularization $\tilde{B} = 10^{-\log_{10}(B)-8}$. Increasing \tilde{B} increases the effect of the spatial regularization.

Figure 4(a) reports maximum PEs as a function of Laplacian regularization Λ and SVR \tilde{B} . It can be noticed that ELR-DOT provides parameter combinations that result in lower maximum PEs than SVR-DOT, especially with increasing values of Λ and \tilde{B} , i.e., because SVR-DOT becomes very unstable for high values of \tilde{B} (low values of B). This results in a very noisy reconstructed image even when a low level of noise is added to the simulations, as was the case here. In general, regularization is introduced to provide stability to a generally ill-posed problem, generated by the fact that the matrix $J_{[\mu_a(\vec{r}), \mu_s'(\vec{r})]} J_{[\mu_a(\vec{r}), \mu_s'(\vec{r})]}^T$ is typically almost singular. In order to better address this issue, we tested how the regularization parameters Λ and \tilde{B} affected the stability of the procedure for the given energy regularization. Figure 4(b) reports the computed Frobenius norms of G , $\|G\|_F$, for different values of Laplacian regularization Λ and SVR \tilde{B} (smaller values indicate greater stability). Note that the abscissa's origin can be considered the ER-DOT $\|G\|_F$ with $E = 10^{-5}$.

One important conclusion can be derived from Fig. 4. ELR-DOT stabilizes the problem at a given ER-DOT solution (decreasing the Frobenius norm), whereas SVR-DOT does the opposite (increasing the Frobenius norm). This finding indicates that with respect to the stability criterion, preference should be

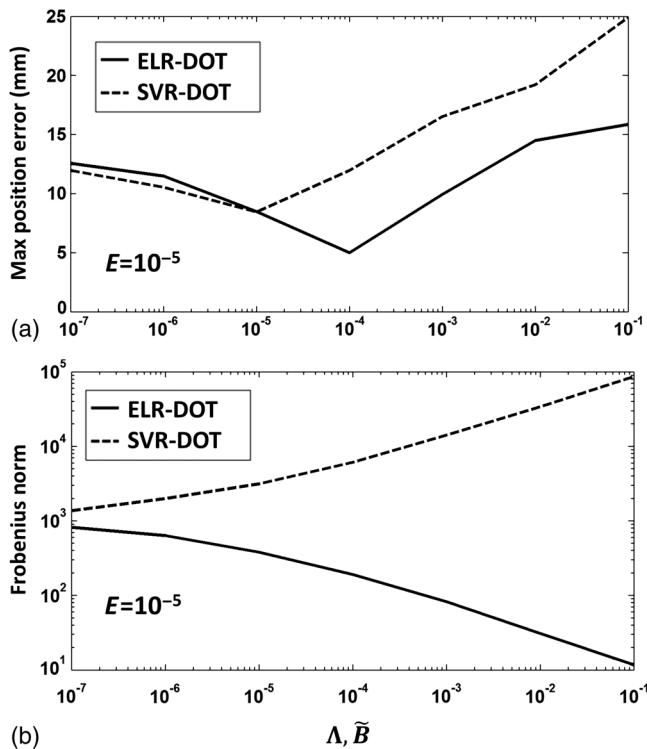


Fig. 4 (a) Maximum PE as a function of the Laplacian regularization parameter Λ and the SVR parameter \tilde{B} at a fixed energy regularization parameter $E = 10^{-5}$. (b) Frobenius norms of the inverse operator G as a function of the Laplacian regularization parameter Λ and the SVR parameter \tilde{B} at a fixed energy regularization parameter $E = 10^{-5}$. The results were obtained with simulations in the slab geometry configuration.

given to ELR-DOT over SVR-DOT when choosing a method for correcting for shallow-depth bias.

Based on the results depicted in Figs. 4(a) and 4(b), and closely matching values independently reported in the literature for SVR-DOT and ER-DOT,^{12,22,23} we chose the optimal regularization parameters as

$$\text{ELR-DOT: } E = 10^{-5}, \Lambda = 10^{-4},$$

$$\text{ER-DOT: } E = 10^{-5},$$

$$\text{SVR-DOT: } E = 10^{-5}, B = 10^{-3} \text{ (derived from } \tilde{B} = 10^{-5} \text{)}.$$

These parameters were optimized for a coarse mesh with 5-mm internode distance. Therefore, optimal values could differ if a different spatial sampling were used. In fact, since the Laplacian operator is defined over space, its effects will vary as a function of internode distance. However, unless the spatial sampling is drastically altered, we do not expect a substantial (i.e., orders of magnitude) change in optimal regularization parameters. Note also that the Frobenius norm value for the chosen parameter is ~ 10 to 15 times lower for ELR-DOT compared to ER-DOT and SVR-DOT, respectively [Fig. 4(b)].

Figure 5 reports the PEs and the FWHMs based on the chosen parameters E , Λ , and B , at different perturbation depths for ELR-DOT, ER-DOT, and SVR-DOT. As can be noticed from this figure, using ER-DOT leads to a low PE in the shallow depth range, with PE increasing linearly for depths > 15 mm. Using SVR-DOT leads to a very low PE (~ 1 mm) in a range between 11 and 23 mm, but, as for the ER-DOT, the PE increases linearly for depths > 23 mm (it also leads to greater

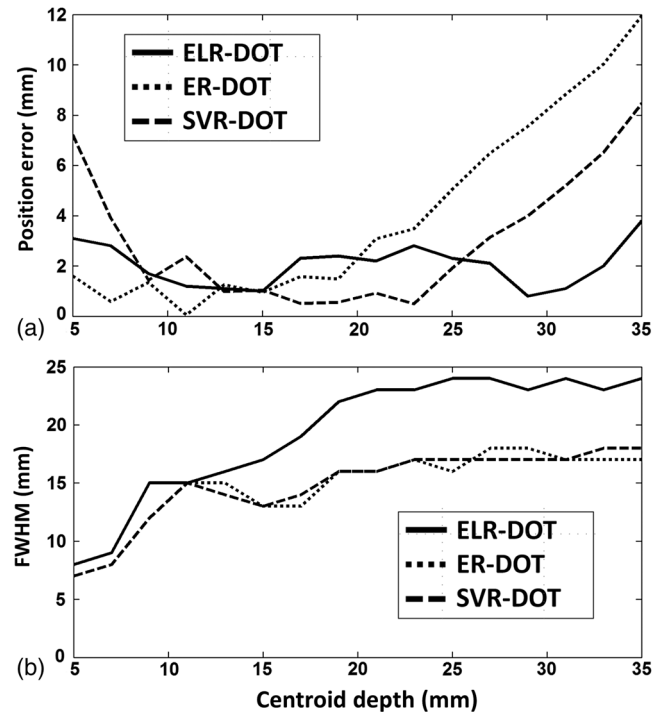


Fig. 5 (a) PEs for ELR-DOT, ER-DOT, and SVR-DOT obtained for perturbation depths between 5 and 35 mm. (b) FWHMs for ELR-DOT, ER-DOT, and SVR-DOT obtained for perturbation depths between 5 and 35 mm. The regularization parameters were ELR-DOT: $E = 10^{-5}$, $\Lambda = 10^{-4}$, ER-DOT: $E = 10^{-5}$, SVR-DOT: $E = 10^{-5}$, $B = 10^{-3}$. The values were obtained during simulations in the slab geometry configuration.

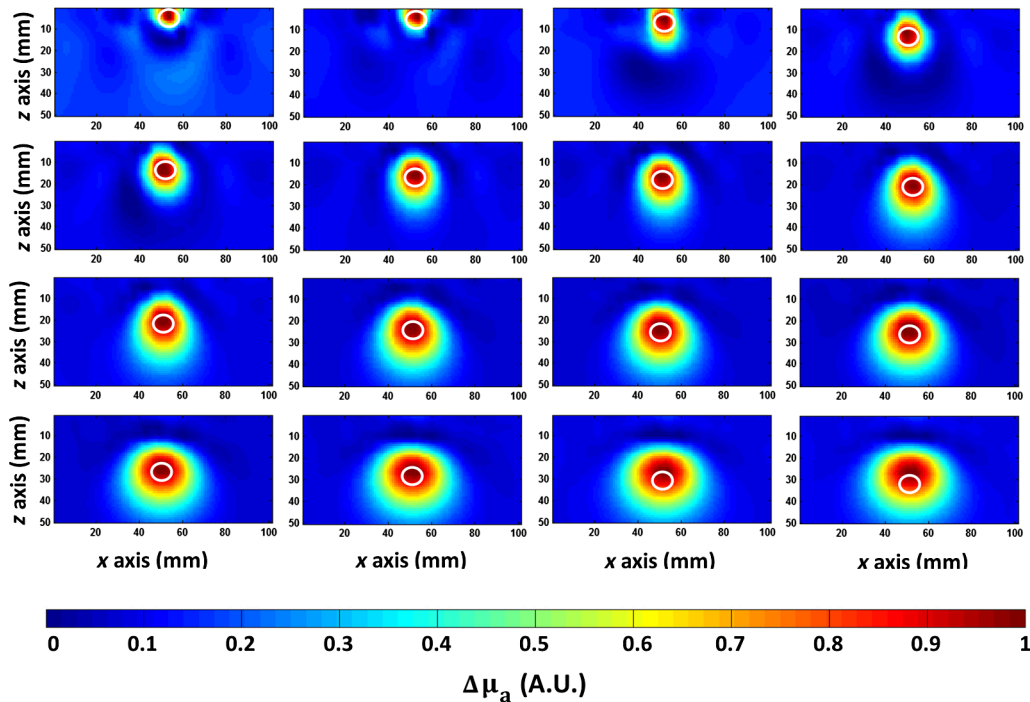


Fig. 6 A single slice of the reconstructed images obtained during simulations for the cube geometry. The slice is perpendicular to the recording surface and passes through the middle of the cube. Perturbation depth (represented by the white circles) increases (moving from left to right and from top to bottom) from a centroid at 5 mm to one at 35 mm, in 2-mm steps. The color scale represents the change in absorption in arbitrary units.

errors for depths <10 mm). ELR-DOT leads to stable PEs (~ 2 to 3 mm) for a wide range of depths (from 5 to 35 mm, i.e., for the entire depth spectrum explored). The FWHMs for the three methods are shown in Fig. 5(b). At greater depths, FWHM increases, with ELR-DOT plateauing around 25 mm and ER-DOT and SVR-DOT plateauing earlier and at a lower overall FWHM.

Taken together, Figs. 4 and 5 clearly show how ELR-DOT trades spatial resolution at deep locations for stability and improved depth localization above 20 mm. However, for a gain of ~ 10 to 15 times in stability ($\|G\|_F$) and a smaller PE across the range of depths (5 to 35 mm), the FWHM of the reconstructed perturbation was increased only by $\sim 30\%$.

In Fig. 6, reconstructed images related to perturbations varying in depths (indicated by white circles) are displayed from left to right and from top to bottom. The minimum depth of the perturbation centroid was 5 mm and the maximum 35 mm, with 2-mm steps. As the figure shows, ELR-DOT follows the perturbation's true location (white circle) accurately for the whole range of depths considered. Only for the last two slices (33 and 35 mm of centroid depth) do the reconstructed perturbation and the real position seem off center. However, what is off center is the maximum value of the reconstructed image. It is clear that the attenuation of the reconstructed perturbation is not symmetric along depths, being more elongated along the horizontal axis for deeper perturbations.

To assess the resolution (as opposed to localization) of ELR-DOT, we performed a simulation based on the same homogeneous slab geometry, considering two perturbations at different lateral separation distances (PD) and a constant depth of 25 mm. The depth was chosen to maximize the FWHM [Fig. 5(b)]; thus, these results are obtained in a "worst-case scenario" of deep perturbations.

Three reconstructed images over a range of PDs at a constant depth are displayed in Fig. 7(a), with their corresponding profiles reported in Fig. 7(b). Clearly, at a distance of 10 mm, the algorithm fuses the two perturbations, whereas at distances of 24 and 36 mm, the algorithm is able to distinguish between them. The parameter used to assess the ability of the algorithm to separate two close perturbations was RP (see Sec. 2.4). Figure 7(c) reports RP as a function of centroid distance of the two perturbations. When RP is equal to or greater than 1,

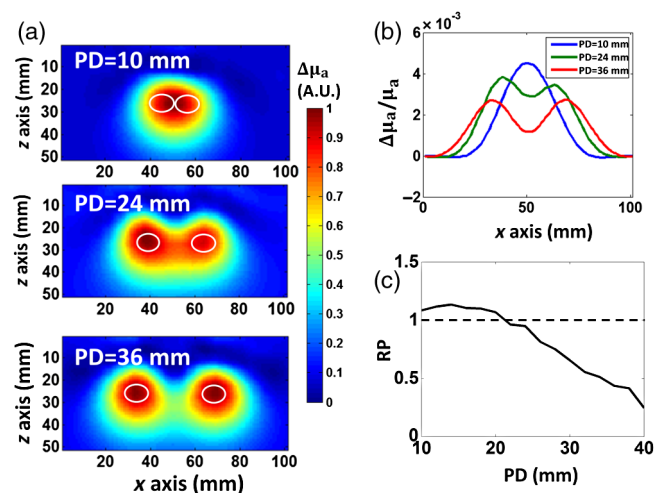


Fig. 7 (a) Reconstructed images (single slice) obtained during simulations with two perturbations at a constant depth (25 mm) in the cube geometry. Perturbations distances (PDs) of 10, 24, and 36 mm are shown. (b) Profiles at 25-mm depth of the reconstructed images for each of the PDs (10, 24, and 36 mm). (c) RP as a function of the PD.

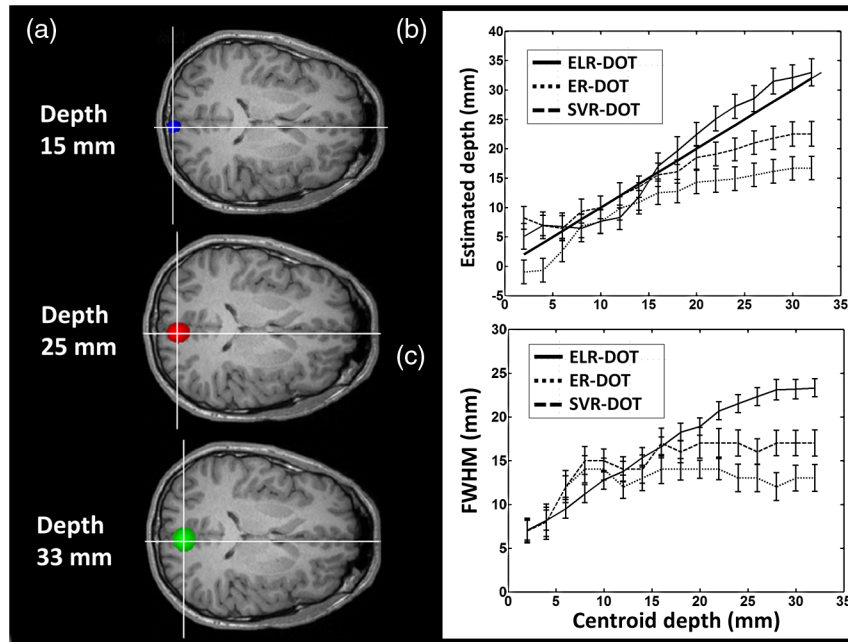


Fig. 8 (a) Example of a reconstructed absorption perturbation for a single subject at a depth of 15 (blue), 25 (red), and 33 mm from the scalp (green). The absorption is reported until an attenuation of 50% from its maximum value (FWHM). The true position of the centroid of the perturbations is displayed by the cross-hair intersections. (b) Average ED and related standard errors across the five subjects as a function of the actual perturbation's centroid depth for ELR-DOT, ER-DOT, and SVR-DOT. (c) Average FWHMs and related standard errors as a function of the actual perturbation's centroid depth for ELR-DOT, ER-DOT, and SVR-DOT. Results were obtained running simulations on heterogeneous head geometry.

the algorithm is not able to separate the two perturbations. Not surprisingly, Fig. 7(c) shows that the minimum distance (considered from the centroids) that allows ELR-DOT to separate them is ~ 22 mm.

3.2 Simulations: Realistic Head Geometry

The stability of the regularization parameters of ELR-DOT, ER-DOT, and SVR-DOT to changes in geometry and baseline optical values was tested using a set of heterogeneous head models obtained from anatomical images of real heads. The head's geometry and optical values were derived from T1-weighted MRIs from five adult subjects. Simulations were conducted by placing optical perturbations at different depths inside the head. A forward solver was computed to estimate the amplitudes of intensity effects using an optical montage positioned over the occipital cortex (Fig. 2). Inverse procedures were performed using tuned regularization parameters derived from the slab geometry simulation.

Figure 8(a) reports examples of reconstructed absorption perturbations using ELR-DOT for a single subject at three depths from the scalp (blue = 15 mm, red = 25 mm, green = 33 mm). The absorption image is thresholded at 50% of its maximum value. The true position of the centroid of the perturbations is displayed by the intersection of the cross. Qualitatively, Fig. 8(a) shows that the ELR-DOT algorithm is able to retrieve the actual position of the perturbation and that the FWHM increases as the depth increases. Figure 8(b) reports the average ED and related standard errors across the five subjects as a function of the actual perturbations centroid depth for ELR-DOT, ER-DOT, and SVR-DOT. No statistically significant discrepancies from the ideal curve were found for

ELR-DOT. Significant underestimation of depth reconstruction was found for ER-DOT and SVR-DOT for depths > 20 mm. Figure 8(c) reports the average FWHM as function of the centroid depth. The FWHM of the reconstructed image increased as the actual depth increased up to a value of ~ 23 mm for ELR-DOT. Similar behavior was found for ER-DOT and SVR-DOT up to a value of ~ 14 to 16 mm. These results are in agreement with the slab geometry simulations and show the stability and accuracy of ELR-DOT in a realistic perturbations medium when compared to ER-DOT and SVR-DOT.

3.3 Phantom Data: Slab Geometry

A phantom study was performed in order to test the ability of the FEM forward solver and the ELR-DOT algorithm to reconstruct optical images. Figure 9(a) reports the ED as function of the centroid depth (mm) for ELR-DOT, ER-DOT, and SVR-DOT. Consistent with the simulations, ELR-DOT showed a nice fit with the ideal curve (solid line), with an average error of ~ 2 mm, and ELR-DOT performed better than ER-DOT and SVR-DOT, especially at greater depths. As expected, based on the simulations, Fig. 9(b) indicates that the FWHM of the reconstructed image is slightly greater for ELR-DOT compared to ER-DOT and SVR-DOT at depths greater than 10 mm.

Figure 10 displays the reconstructed images resulting from placing the absorbing object at different depths (indicated by a white circle) within the homogenous milk medium. The minimum depth of the perturbations centroid was 3 mm, the maximum 33 mm with 2-mm steps. Although the images were obtained for a $100 \times 100 \times 100$ mm cube, the images are shown up to a depth of 50 mm for display purposes. These real images are noisier than the simulated images reported in Fig. 6.

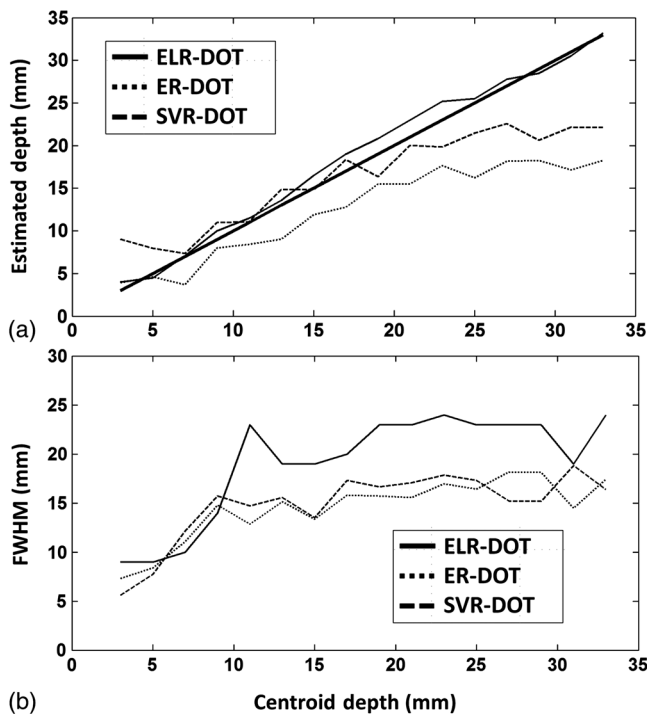


Fig. 9 (a) EDs as a function of the actual perturbation's centroid depth for ELR-DOT, ER-DOT, and SVR-DOT. (b) FWHMs as a function of the actual perturbation's centroid depth for ELR-DOT, ER-DOT, and SVR-DOT. Results were obtained using real (phantom) data in the slab geometry configuration.

However, they show that the ELR-DOT method accurately retrieved the true perturbations' location (white circle) for all the depths considered (up to 33 mm).

3.4 Real (In-Vivo) Data: Eccentricity Study

Finally, to test the ability of ELR-DOT to localize functional activation *in vivo*, we compared the depth localization of brain activity obtained with fMRI and ELR-DOT for a subject undergoing a visual eccentricity task. Figure 11 reports a mapping of the brain response, measured with fMRI [Fig. 11(a)] and ELR-DOT [Fig. 11(b)], as a function of the visual angle of stimulation $VA(x, y, z)$ on a particular axial slice overlaid onto the subject's anatomical image. $VA(x, y, z)$ is displayed only for statistically significant voxels ($p < 0.05$, unadjusted for multiple comparisons). Colors represent the visual angle at which the response was maximal, coded according to a color scale presented in Fig. 11(c). The fMRI results [Fig. 11(a)] showed the characteristic spatial organization of the visual cortex as function of the eccentricity of the visual stimulation. This organization consists of a progressively deeper response for more eccentric stimuli. Figure 11(b) reports the same image obtained by applying ELR-DOT to 830-nm optical intensity fNIRS data. The volume of the significantly activated region is smaller for fNIRS when compared to fMRI. This result reflects the lower signal-to-noise ratio, the masking procedure for deep regions, and the limited optode coverage for lateral activations in DOT. The loss of very superficial activations for ELR-DOT when compared to fMRI is caused by the subtraction of short channels (at 20-mm interfiber distance) to compensate for systemic fluctuations. However, qualitatively, the two maps show strong similarities. To quantify them, we first masked

the fMRI locations to match the more limited area showing activation with ELR-DOT [see black tracing in Figs. 11(a) and 11(b)]. We then divided the area into four ROIs, the boundaries of which were defined by the visual angle (2.5 deg, 2.5 to 5.0 deg, 5.0 to 7.5 deg, and 7.5 to 10.0 deg), which optimally activated each voxel in the ELR-DOT data (i.e., the ROIs encompassed four receptive field ranges). The centroid (in degrees of angle) of the receptive field was estimated as the average visual angle associated with the maximum response for each voxel in a given ROI (the same operation was computed for ELR-DOT data). Figure 11(d) shows a scatterplot of the two estimates of the receptive field's centroids for each ROI (estimates based on ELR-DOT on the abscissa and on fMRI on the ordinate). The data show a very good correlation between the centroids of the receptive fields obtained with the two techniques ($r = 0.95$, $p = 0.04$). Across the four ROIs, the largest mismatch between fMRI- and ELR-DOT-based receptive field centroids was ~ 2 deg. This is translated into a maximum mismatch of ~ 4 mm in depth estimation between the two methods. Importantly, the maximum depth of the ELR-DOT activated area from the surface of the scalp was 33 mm. These results support the claim that (1) ELR-DOT provides depth estimates that closely correspond with those obtained with fMRI, the gold-standard for 3-D functional imaging *in vivo*, and (2) ELR-DOT can accurately localize brain activity up to a depth of 30 to 33 mm from the surface of the scalp.

4 Discussion

In this paper, we introduced a new method for the 3-D reconstruction of DOT data (ELR-DOT). We also compared ELR-DOT with two previously described methods (ER-DOT and SVR-DOT) based on their ability to accurately retrieve the depth of absorption effects (PE) within the brain, as well as on the stability of the estimate (Frobenius norm). This latter metric is important because unstable solutions cannot be relied upon, especially under noisy conditions, or under conditions in which the forward model is even marginally incorrect.

Prior to this comparison, we first fine-tuned the parameters used for SVR-DOT and ELR-DOT. To this end, we used simulated data (based on a homogenous medium with simple geometry) to generate forward models based on an absorbing object located at different depths, varied the relevant parameters used by these inverse procedures over a very broad range of depths, and estimated the PE and Frobenius norm for each case. In addition to parameter tuning, this analysis indicated two significant advantages of ELR-DOT relative to SVR-DOT: ELR-DOT produces a smaller minimum PE and more stable results [i.e., a smaller Frobenius norm—see Fig. 4(b)]. Thus, ELR-DOT can be expected to be less sensitive to noisy conditions and to errors in the forward model than the other techniques examined. Importantly, the parameters computed using this analysis were then applied in all subsequent tests.

A second set of analyses were based on a more complex geometry simulating a real head, based on realistic absorption and scattering parameters for various types of tissues, and small, slightly absorbing objects varying in depth between 3 and 33 mm. These simulations suggest that ELR-DOT can accurately retrieve the depth of absorbing objects at least up to the maximum depth explored (33 mm). By contrast, SVR-DOT can only do that for depths ranging between 8 and 20 mm, and ER-DOT tends to underestimate the depth of objects at any depth. The accuracy advantage of ELR-DOT, however, was

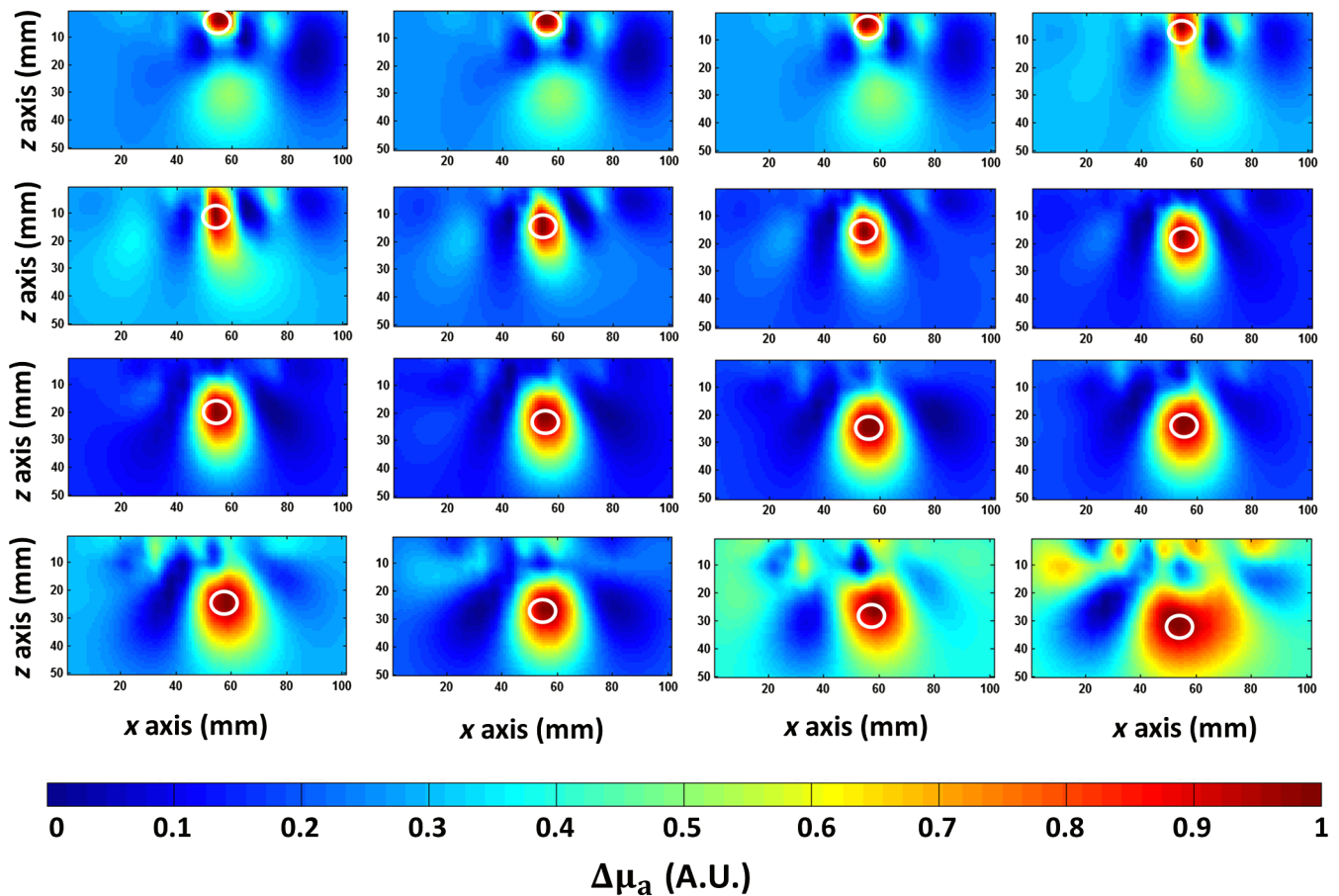


Fig. 10 Slices of the reconstructed image obtained for real (phantom) data collected with the homogenous slab geometry. Each slice is perpendicular to the recording surface and is passing through the middle of the cube. Perturbation depth (represented by the white circles) increases (moving from left to right and from top to bottom) from a centroid at 3 to 33 mm in 2-mm steps. The color scale represents the change in absorption in arbitrary units.

accompanied by a loss of resolution at greater depths (30%). Moreover, these simulations demonstrated that the parameters derived from the homogeneous model also worked well in more complex inhomogeneous geometries, with somewhat different optical properties. Although we did not explore a wide range of geometries and optical values, these results suggest that the tuned parameters are likely to be stable and appropriate for the typical conditions occurring in most fNIRS studies.

A third set of analyses tested these procedures using actual data based on a homogenous-medium phantom experiment with simple geometry (again varying the depth of a small, slightly absorbing object located inside the medium). The results of this phantom experiment were virtually identical to those obtained with the simulations, even though the actual data were noisier. Again, ELR-DOT produced accurate estimates of the depth of the absorbing object up to the maximum depth explored (33 mm), with SVR-DOT only retrieving depth accurately up to a depth of 22 mm, and ER-DOT always underestimating the depth of the object. We also replicated the resolution data, with ELR-DOT showing some loss in resolution as the objects became deeper.

In order to test the feasibility of using the procedure with *in-vivo* data, we applied the algorithm to data from one subject in an actual functional brain activation study. We used the eccentricity of visual stimuli to manipulate the depth of the activated

brain area (as greater stimulus eccentricities are represented in deeper regions of visual cortex). The exact location of the activated areas was estimated with a separately recorded fMRI study using the same visual stimulation on the same subject. On this particular subject, ELR-DOT provided an accurate reconstruction of the depth of the active brain area, up to a depth of ~ 33 mm.

The data also indicated that ELR-DOT is an accurate and unbiased method for retrieving the depth of an absorbing object over a wide range of depths. Importantly, it does so without sacrificing the stability of the results, a problem instead existing for SVR-DOT, which makes the latter very sensitive to errors in the forward model and to noise in the data. ER-DOT did not perform well in general, tending to underestimate the depth of the absorbers, a problem that was predicted on theoretical grounds. The major negative aspect of ELR-DOT was a loss in resolution at large depths.

The estimate of the maximum depth that can be explored applying ELR-DOT to scalp-recorded fNIRS (~ 30 mm) surpasses those obtained with current methods, such as ER-DOT and SVR-DOT, neither of which can accurately localize absorbing phenomena occurring at depths exceeding 20 mm. Of course, accurate depth estimation requires concurrent recording from a large number of channels,¹⁰ so that not only can different scalp locations be measured at the same time, the same locations

can also be explored by a large number of channels with different source–detector distances.⁴⁸

An example of the potential advantages provided by accurate 3-D reconstruction is given by the data presented in Fig. 11. Here, we show that it is feasible to apply ELR-DOT to fNIRS data. ELR-DOT allowed us to generate a retinotopic map of the primary visual cortex of a quality comparable to that obtained on the basis of fMRI data. However, these data also show that fNIRS provides data within a more restricted area of the brain than fMRI. This more limited range can be attributed to three factors: (1) the montage used for recording fNIRS did not completely cover lateral occipital areas; (2) fNIRS is not sensitive to phenomena deeper than 30 to 33 mm; and (3) a portion of the most superficial fNIRS signal was canceled by the regression method used to clean up the signal of nonbrain phenomena. While the first and third factors could be improved upon in future recordings using more appropriate montages, we believe that the depth limit of fNIRS is much more difficult to overcome.

In the current paper, the 3-D reconstruction of brain activation data was based on analyses performed using data recorded at a single wavelength (830 nm). Although this procedure has been used before,⁵⁵ it is general practice in fNIRS studies to use a combination of a short (650 to 700 nm) and a long (800 to 900 nm) wavelength to separately estimate changes in concentration of each hemoglobin species (oxy- and deoxyhemoglobin). However, when the interest is in depth estimation and 3-D reconstruction, we need to consider that the basic optical properties (and depth penetration) vary across these two basic wavelengths. Thus, it is inappropriate to perform the 3-D reconstruction on oxy- and deoxyhemoglobin transformations.

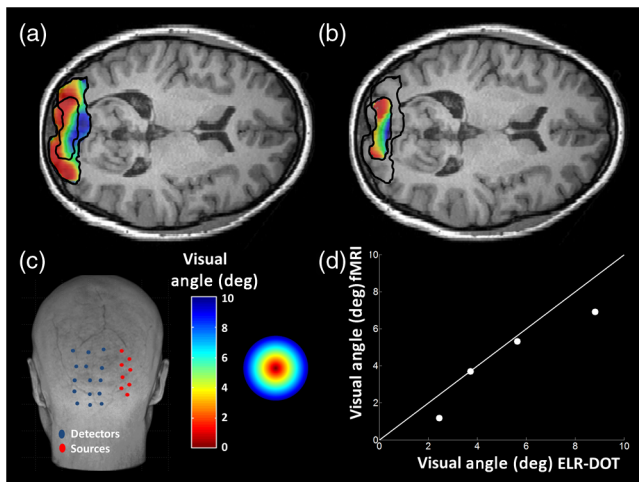


Fig. 11 (a) fMRI: colors represent activation correlated with different visual angles overlaid on an axial anatomical slice through primary visual cortex (significant voxels, $p < 0.05$, uncorrected). Black contours define statistically activated regions for both fMRI and ELR-DOT. (b) ELR-DOT: colors represent activation correlated with different visual angles overlaid on an axial anatomical slice through primary visual cortex (significant voxels, $p < 0.05$, uncorrected). Black contours define statistically activated regions for both fMRI and ELR-DOT. (c) Actual digitized montage used for the optical recording (rear view of the head): the sources are indicated in blue and the detectors in red—all combinations of sources and detectors were used. (d) Scatterplot of the average visual angle in four ROIs for ELR-DOT and the average visual angle for the corresponding fMRI regions ($r = 0.95$, $p = 0.04$). The color coding for the different visual angles is presented in bar graph (c).

Rather, the correct approach is to perform two separate 3-D reconstructions (one for the shorter and one for the longer wavelengths) and then use the 3-D reconstructed data to estimate the changes in hemoglobin species concentration. Further, it should be noted that when the interest is only in the localization of brain activation effects (and not in their quantification), the 3-D maps obtained at 830 nm are likely to be closely correlated with those related to the BOLD fMRI signal. This occurs because (1) the longer wavelength (830 nm) is more sensitive to oxyhemoglobin than to deoxyhemoglobin (ratio $\sim 3/2$)⁵⁶ and (2) the BOLD effect causes a bigger variation in oxyhemoglobin compared to deoxyhemoglobin (ratio $\sim 3/1$).⁵⁷ In practice, probably because of the higher baseline absorption (and therefore lesser penetration of photons) of biological tissues in the shorter wavelength range, we found that using a single longer wavelength increases the SNR of the measurements. This procedure can be employed when localization, rather than hemoglobin estimation (or differentiation between different types of signals), is the target of the analysis, and it is particularly crucial for deep perturbation estimation (where the noise level is high). However, if it is critical to obtain quantitative estimates of hemoglobin concentration, the procedure can, in principle, be repeated at both wavelengths, and changes in oxy- and deoxyhemoglobin concentration could be computed based on the estimated absorption effects obtained for each wavelength. It can be expected, however, that this may result in loss of accuracy at deep locations.

It should be noted that this paper only investigates which regularization procedure produces the best depth estimates of absorption effects within the brain. However, as we mentioned earlier, the inverse solution builds upon the results of the forward solution. In this sense, the best inverse solution procedure can only produce results as good as the accuracy that the forward solution permits. Any inaccuracy in the forward model will be reflected in errors in the inverse solution. The amount of error introduced by an erroneous forward solution can change, however, based on the stability of the inverse procedure, with less stable inverse procedures amplifying the error. To evaluate the quality of the forward model in our study, we can only consider the phantom and brain activation data on one subject, as all the simulations were based on knowing the forward solution exactly. In our study, the accuracy of the inverse solution obtained with ELR-DOT indicates that the forward model was adequate for a homogenous medium and was also adequate for the real-brain functional activation data on one subject. The accuracy of the forward model is particularly important for clinical and experimental applications in humans. Further studies are required to establish the optimal forward solution for each particular application, as this may interact with the optical properties of tissue. It should be noted that a large variability in the baseline optical properties of human head tissues has been reported in the literature.⁵⁸

The regularization method employed here includes elements of the two most commonly used regularization methods used for ERPs, MEG, and EEG source analysis. The relative merits of minimum norm and LORETA as tools for conducting source analysis of electrophysiological data have been previously investigated.²⁸ These previous studies have indicated that LORETA is in fact superior to minimum-norm approaches in localizing deep sources—a result consistent with our finding that ER-DOT is not very good in this case—but does not necessarily confer an advantage at accurately localizing superficial sources, where instead there is a clear loss in resolution.

A known limitation of LORETA when applied to electrophysiological data is the loss of spatial resolution as the number of concurrent electrical sources increases. This problem is exacerbated by the large spreading of electrical signals across the brain due to volume conduction. We expect this issue to be less problematic for DOT because the optical signal decays faster with distance than the electric field (i.e., exponentially rather than in a quadratic manner). Consistent with this expectation, in the current study, we tested the ELR-DOT algorithm using two optical perturbations and found a reasonable separation of each perturbation (and little cross-talk) when the distance between them was 24 mm or greater. Thus, we expect that if perturbations are not too close to each other, ELR-DOT should be able to accurately describe a number of them at the same time.

Here, we considered a form of ℓ_2 -norm regularization with *a-priori* tuned regularization parameters. This inverse procedure allows us to obtain a closed-form solution, which is independent of the measured data. Other studies based on iterative procedures and/or sparsity constraints have shown improved lateral resolution or localization accuracy of DOT data.^{59–62}

However, these methods do not provide a closed-form solution and they are not data independent. Here, we demonstrated that by adding a Laplacian regularization to the ℓ_2 regularized solution, it is possible to obtain perturbation localization and robustness to changes in the types of geometry and optical conditions typically occurring in DOT recordings. This performance was obtained while increasing the stability of the inverse procedure.

We found that our combined ELR-DOT approach, while providing unbiased depth estimates across a wide range of depths, does in fact lose some spatial resolution with respect to ER-DOT and SVR-DOT. A trade-off between accuracy of depth estimation and resolution is probably unavoidable when using general approaches such as those described here, and in these cases, the investigators need to choose the lesser of two evils (a fuzzier solution versus an incorrect one). An alternative approach is to introduce additional constraints based on anatomical or other information. A problem with this alternative approach is that it is not always clear how valid and generalizable these constraints are. The approach presented in this paper is more general and can help identify extracerebral components of fNIRS recording. It can also be applied to a broader spectrum of DOT data. In summary, using an energy and Laplacian ℓ_2 regularization procedure with tuned regularization parameters, we were able to obtain a stable and accurate closed-form solution of the inverse DOT problem that showed stability to change in geometry and optical properties typically encountered in brain DOT. The energy/Laplacian regularization algorithm was also tested in a phantom study where an absorption perturbation was varied in depth in a homogeneous medium. A good correspondence with simulations was obtained, supporting the simulation results. Finally, the possibility of applying this method *in vivo* was tested by comparing fMRI and ELR-DOT data for a single subject who underwent a typical visual eccentricity study. A good correspondence was obtained between fMRI and ELR-DOT results. ELR-DOT could provide robust, unbiased depth estimation of fNIRS data up to a depth of ~30 to 33 mm in the adult human head. The Laplacian regularization scheme can be considered a useful mathematical tool when accurate depth estimation is preferred over lateral resolution of diffuse optical data.

Acknowledgments

This work was supported by grants from NIH 5R56MH097973 (Drs. G.G. and M.F., PIs) and S10-RR029294 (Dr. G.G., PI). We wish to thank Ben Zimmerman for help with data collection and preprocessing of fNIRS and fMRI data.

References

1. G. Boas, "Noninvasive imaging of the brain," *Opt. Photonics News* **15**(1), 52–55 (2004).
2. A. P. Gibson, J. C. Hebden, and S. R. Arridge, "Recent advances in diffuse optical imaging," *Phys. Med. Biol.* **50**(4), R1 (2005).
3. A. Villringer and B. Chance, "Non-invasive optical spectroscopy and imaging of human brain function," *Trends Neurosci.* **20**(10), 435–442 (1997).
4. Y. Hoshi and M. Tamura, "Dynamic multichannel near-infrared optical imaging of human brain activity," *J. Appl. Physiol.* **75**(4), 1842–1846 (1993).
5. A. Villringer et al., "Near infrared spectroscopy (NIRS): a new tool to study hemodynamic changes during activation of brain function in human adults," *Neurosci. Lett.* **154**(1), 101–104 (1993).
6. D. A. Boas, A. M. Dale, and M. A. Franceschini, "Diffuse optical imaging of brain activation: approaches to optimizing image sensitivity, resolution, and accuracy," *Neuroimage* **23**, S275–S288 (2004).
7. A. T. Eggbrecht et al., "A quantitative spatial comparison of high-density diffuse optical tomography and fMRI cortical mapping," *Neuroimage* **61**(4), 1120–1128 (2012).
8. N. M. Gregg et al., "Brain specificity of diffuse optical imaging: improvements from superficial signal regression and tomography," *Front. Neuroeng.* **2** (2010).
9. B. R. White and J. P. Culver, "Phase-encoded retinotopy as an evaluation of diffuse optical neuroimaging," *Neuroimage* **49**(1), 568–577 (2010).
10. B. W. Zeff et al., "Retinotopic mapping of adult human visual cortex with high-density diffuse optical tomography," *Proc. Natl. Acad. Sci.* **104**(29), 12169–12174 (2007).
11. Y. Zhan et al., "Image quality analysis of high-density diffuse optical tomography incorporating a subject-specific head model," *Front. Neuroeng.* **4** (2012).
12. A. T. Eggbrecht et al., "Mapping distributed brain function and networks with diffuse optical tomography," *Nat. Photonics* **8**(6), 448–454 (2014).
13. H. Dehghani et al., "Near infrared optical tomography using NIRFAST: algorithm for numerical model and image reconstruction," *Commun. Numer. Methods Eng.* **25**(6), 711–732 (2009).
14. M. A. Franceschini and D. A. Boas, "Noninvasive measurement of neuronal activity with near-infrared optical imaging," *Neuroimage* **21**(1), 372–386 (2004).
15. O. Lee, S. Tak, and J.C. Ye, "A unified sparse recovery and inference framework for functional diffuse optical tomography using random effect model," *IEEE Trans. Med. Imaging* **34**(7), 1602–1615 (2015).
16. J. N. Reddy, *An Introduction to the Finite Element Method*, Vol. 2, McGraw-Hill, New York (1993).
17. S. R. Arridge, "Optical tomography in medical imaging," *Inverse Probl.* **15**(2), R41 (1999).
18. D. A. Boas and A. M. Dale, "Simulation study of magnetic resonance imaging-guided cortically constrained diffuse optical tomography of human brain function," *Appl. Opt.* **44**(10), 1957–1968 (2005).
19. R. L. Barbour et al., "MRI-guided optical tomography: prospects and computation for a new imaging method," *Comput. Sci. Eng.* **2**, 63–77 (1995).
20. M. Guven et al., "Diffuse optical tomography with a priori anatomical information," *Phys. Med. Biol.* **50**(12), 2837 (2005).
21. X. Intes et al., "Diffuse optical tomography with physiological and spatial a priori constraints," *Phys. Med. Biol.* **49**(12), N155 (2004).
22. J. P. Culver et al., "Volumetric diffuse optical tomography of brain activity," *Opt. Lett.* **28**(21), 2061–2063 (2003).
23. H. Dehghani et al., "Depth sensitivity and image reconstruction analysis of dense imaging arrays for mapping brain function with diffuse optical tomography," *Appl. Opt.* **48**(10), D137–D143 (2009).

24. V. C. Kavuri et al., "Sparsity enhanced spatial resolution and depth localization in diffuse optical tomography," *Biomed. Opt. Express* **3**(5), 943–957 (2012).
25. H. Niu et al., "Comprehensive investigation of three-dimensional diffuse optical tomography with depth compensation algorithm," *J. Biomed. Opt.* **15**(4), 046005 (2010).
26. B. W. Pogue et al., "Spatially variant regularization improves diffuse optical tomography," *Appl. Opt.* **38**(13), 2950–2961 (1999).
27. F. Tian and H. Liu, "Depth-compensated diffuse optical tomography enhanced by general linear model analysis and an anatomical atlas of human head," *NeuroImage* **85**, 166–180 (2014).
28. R. D. Pascual-Marqui et al., "Functional imaging with low resolution brain electromagnetic tomography (LORETA): review, new comparisons, and new validation," *Jpn. J. Clin. Neurophysiol.* **30**, 81–94 (2002).
29. R.D. Pascual-Marqui, C.M. Michel, and D. Lehmann, "Low resolution electromagnetic tomography: a new method for localizing electrical activity in the brain," *Int. J. Psychophysiol.* **18**(1), 49–65 (1994).
30. R. D. Pascual-Marqui et al., "Imaging the electrical neuronal generators of EEG/MEG," In *Electrical Neuroimaging*, pp. 49–78, C. M. Michel et al., Eds., Cambridge University Press, New York (2009).
31. A. Ishimaru, "Diffusion of light in turbid material," *Appl. Opt.* **28**(12), 2210–2215 (1989).
32. K. D. Paulsen and H. Jiang, "Spatially varying optical property reconstruction using a finite element diffusion equation approximation," *Med. Phys.* **22**(6), 691–701 (1995).
33. H. Dehghani et al., "Near infrared optical tomography using NIRFAST: algorithm for numerical model and image reconstruction," *Commun. Numer. Methods Eng.* **25**(6), 711–732 (2009).
34. L. Y. Chen, M. C. Pan, and M. C. Pan, "Implementation of edge-preserving regularization for frequency-domain diffuse optical tomography," *Appl. Opt.* **51**(1), 43–54 (2012).
35. J. Prakash et al., "Model-resolution-based basis pursuit deconvolution improves diffuse optical tomographic imaging," *IEEE Trans. Med. Imaging* **33**(4), 891–901 (2014).
36. Q. Fang and D. Boas, "Tetrahedral mesh generation from volumetric binary and grayscale images," in *IEEE Int. Symp. on Biomedical Imaging: From Nano to Macro*, pp. 1142–1145, IEEE (2009).
37. W. D. Penny et al., eds. *Statistical Parametric Mapping: The Analysis of Functional Brain Images*, Academic Press, San Diego, California (2011).
38. S. R. Arridge and M. Schweiger, "Photon-measurement density functions. Part 2: Finite-element-method calculations," *Appl. Opt.* **34**(34), 8026–8037 (1995).
39. A. N. Tikhonov and A. I. Arsenin, *Solutions of Ill-Posed Problems*, pp. 258, Halsted Press, New York (1977).
40. G. H. Golub, M. Heath, and G. Wahba, "Generalized cross-validation as a method for choosing a good ridge parameter," *Technometrics* **21**(2), 215–223 (1979).
41. P. C. Hansen, "Analysis of discrete ill-posed problems by means of the L-curve," *SIAM Rev.* **34**(4), 561–580 (1992).
42. L. N. Trefethen and D. Bau III, *Numerical Linear Algebra*, Vol. **50**, Siam, Philadelphia (1997).
43. S. L. Jacques, "Optical properties of biological tissues: a review," *Phys. Med. Biol.* **58**(11), R37 (2013).
44. C. Rorden, dcm2nii DICOM to Nifti conversion. The source for neuroimaging: MRICoron, 2009, <http://www.mccauslandcenter.sc.edu/mricor/mricron/dcm2nii.html>.
45. A. M. Chiarelli et al., "Comparison of procedures for co-registering scalp-recording locations to anatomical magnetic resonance images," *J. Biomed. Opt.* **20**(1), 016009 (2015).
46. M. D. Waterworth et al., "Optical transmission properties of homogenised milk used as a phantom material in visible wavelength imaging," *Australas. Phys. Eng. Sci. Med.* **18**(1), 39–44 (1995).
47. J. H. Choi et al., "Noninvasive determination of the optical properties of adult brain: near-infrared spectroscopy approach," *J. Biomed. Opt.* **9**(1), 221–229 (2004).
48. G. Gratton et al., "Toward noninvasive 3-D imaging of the time course of cortical activity: investigation of the depth of the event-related optical signal," *NeuroImage* **11**(5), 491–504 (2000).
49. E. Maclin et al., "Retinotopic map on the visual cortex for eccentrically placed patterns: first noninvasive measurement," *Il Nuovo Cimento D* **2**(2), 410–419 (1983).
50. B. A. Wandell, "Computational neuroimaging of human visual cortex," *Ann. Rev. Neurosci.* **22**(1), 145–173 (1999).
51. S. D. Slotnick and S. Yantis, "Efficient acquisition of human retinotopic maps," *Hum. Brain Mapp.* **18**(1), 22–29 (2003).
52. A. M. Chiarelli et al., "A kurtosis-based wavelet algorithm for motion artifact correction of fNIRS data," *NeuroImage* **112**, 128–137 (2015).
53. R. B. Saager, N. L. Telleri, and A. J. Berger, "Two-detector corrected near infrared spectroscopy (C-NIRS) detects hemodynamic activation responses more robustly than single-detector NIRS," *NeuroImage* **55**(4), 1679–1685 (2011).
54. M. I. Sereno et al., "Borders of multiple visual areas in humans revealed by functional magnetic resonance imaging," *Science* **268**(5212), 889–893 (1995).
55. A.M. Chiarelli et al., "Fast optical signal in visual cortex: improving detection by general linear convolution model," *NeuroImage* **66**, 194–202 (2013).
56. N. Kollias and W. B. Gratzler, *Tabulated Molar Extinction Coefficient for Hemoglobin in Water*, Wellman Laboratories, Harvard Medical School, Boston (1999).
57. T. J. Huppert et al., "A temporal comparison of BOLD, ASL, and NIRS hemodynamic responses to motor stimuli in adult humans," *NeuroImage* **29**(2), 368–382 (2006).
58. A. Farina et al., "In-vivo multilaboratory investigation of the optical properties of the human head," *Biomed. Opt. Express* **6**(7), 2609–2623 (2015).
59. F. Abdelnour, C. Genovese, and T. Huppert, "Hierarchical Bayesian regularization of reconstructions for diffuse optical tomography using multiple priors," *Biomed. Opt. Express* **1**(4), 1084–1103 (2010).
60. M. Jacob et al., "Level-set algorithm for the reconstruction of functional activation in near-infrared spectroscopic imaging," *J. Biomed. Opt.* **11**(6), 064029 (2006).
61. V. C. Kavuri, Z. J. Lin, and H. Liu, "Comparison of L1 and L2 regularizations in diffuse optical tomography," *Biomed. Opt., BTu3A.22* (2012).
62. T. Shimokawa et al., "Hierarchical Bayesian estimation improves depth accuracy and spatial resolution of diffuse optical tomography," *Opt. Express* **20**(18), 20427–20446 (2012).

Antonio M. Chiarelli is a research associate in the Cognitive Neuroimaging Lab at the Beckman Institute at University of Illinois. He received his BS and MS degrees in physics engineering, optics and photonics from the Milan Polytechnic in Milan, Italy, in 2006 and 2009, respectively. In 2013, he received his PhD in neuroimaging technologies from the University of G. D'Annunzio in Chieti-Pescara, Italy. His research interests focus on functional optical brain imaging methods (including hardware, analytic developments, and applications).

Edward L. Maclin received his PhD from the New York University in 1983. He is a research assistant professor at the Beckman Institute, University of Illinois. Following his postdoctoral fellowship at Mount Sinai Hospital/CUNY, he directed the electrophysiology laboratory in the Department of Biological Psychiatry at the New York State Psychiatric Institute/Columbia University. From 1989 to 1997, he was technical director of the Center for Magnetoencephalography at the Albuquerque Veterans Medical Center. He joined the Cognitive Neuroimaging Laboratory in 1997.

Kathy A. Low received her PhD from the University of Missouri in 1997. She has extensive experience in multimodal imaging, including diffuse optical imaging, electrophysiology, and structural and functional MRI techniques. For the past 13 years, she has served as a senior research scientist in the Cognitive Neuroimaging Lab, coordinating and implementing many large-scale multimodal imaging studies involving participants from infants to old age.

Kyle E. Mathewson is an assistant professor in the Department of Psychology and Neuroscience, and Mental Health Institute at the University of Alberta. He was a postdoctoral fellow at the Beckman Institute at the University of Illinois. He received his PhD in 2011 from the University of Illinois, and his BA degree from the University of Victoria in 2007. His research uses human behavioural studies, neuroimaging, optical imaging, and electrophysiological recording to gain understanding of the visual attention system.

Monica Fabiani is a professor of psychology and neuroscience at the University of Illinois, and a faculty at the Beckman Institute. She received her PhD in biological psychology from the University of Illinois (1990). She cochaired the Biological Intelligence Group at the Beckman Institute (2005 to 2010) and was the president of the Society for Psychophysiological Research (2007 to 2008). She is the editor of the journal *Psychophysiology*, and a fellow of the Association for Psychological Science.

Gabriele Gratton received his MD degree from the University of Rome in 1980 and his PhD from the University of Illinois in 1991. He is a professor of psychology and neuroscience at the University of Illinois. He received the Provost Outstanding Junior Faculty Research Award from the University of Missouri and the Early Career Award from the Society for Psychophysiological Research (SPR). He is a fellow of the Association for Psychological Science, and was the president of SPR in 2010.